ChemComm

ROYAL SOCIETY OF CHEMISTRY

COMMUNICATION

View Article Online
View Journal | View Issue

Check for updates

Cite this: *Chem. Commun.*, 2024, **60**, 13955

Received 1st September 2024,
Accepted 1st November 2024

DOI: 10.1039/d4cc04496g

rsc.li/chemcomm

Template-directed synthesis of one-dimensional hexagonal PdTe nanowires for efficient ethanol electrooxidation†

Zhenya Hu,[ab] Mengyuan Ma,[ab] Penglei Cui,[a] Hui Liu,[a] Dong Chen,[a] Shaonan Tian,*[a] Lin Xu*[c] and Jun Yang[ab]

A template-directed synthesis of one-dimensional hexagonal PdTe nanowires using Te nanowires as a template through a two-step hydrothermal process is developed, which exhibit excellent mass activity of 4.4 A mg_{Pd}^{-1} for ethanol electrooxidation in an alkaline medium. This work enriches the controlled synthesis of one-dimensional noble metal chalcogenide nanomaterials.

Direct ethanol fuel cells are promising as next-generation power sources due to their high energy density and environmental friendliness.[1] Developing cost-effective and high-efficiency electrocatalysts for the ethanol oxidation reaction (EOR) is critical for advancing DEFC technology.[2] Palladium (Pd)-based nanomaterials have emerged as viable alternatives to expensive platinum (Pt) for promoting the EOR in an alkaline medium.[3] Pd alloys with oxyphilic base metals like Zn, Sb, Sn and Bi have shown enhanced EOR activity due to the presence of Pd–metal dual sites,[4] of which the oxyphilic metal sites facilitate the removal of poisonous CO and CH_x species generated during the EOR process through the adsorbed OH_{ads} species, thereby improving their EOR catalysis.[5] Furthermore, incorporating less expensive non-metal atoms such as chalcogenides (S, Se and Te) can not only adjust the intermediate adsorption to promote CO oxidation but also modulate the electronic structure of Pd, enhancing the cleavage of the C–C bond.[6]

Engineering the morphology of noble metal-based nanomaterials is another effective way to boost their electrocatalysis by maximizing the exposure of active sites while minimizing the consumption of precious metals.[7] Well-defined tellurium (Te) nanomaterials can be precisely controlled and synthesized, serving as ideal templates for fabricating composition-tunable nanocatalysts.[8] As a typical example, quaternary PtPdRuTe nanotubes with optimized incorporation of Pd were synthesized using ultrathin Te nanowires (denoted as Te NWs) as sacrificial templates, which exhibit enhanced activity and stability toward the methanol oxidation reaction.[9] Recently, another work associated with the synthesis of one-dimensional (1D) Ir–Te porous nanowires using Te NWs as a template has also been reported.[10]

Herein, we present a template-directed synthesis of 1D PdTe nanowires (denoted as PdTe NWs) for achieving superior EOR electrocatalysis. Different from a previous report that Pd–Te nanotubes were synthesized by a galvanic displacement between Te NWs and H_2PdCl_4 at the expense of the Te NWs in ethylene glycol (EG) at low temperature,[11] PdTe NWs with a homogeneous hexagonal crystal phase were successfully synthesized using a high-temperature polyol system in this study. Profiting from their 1D morphology and unique crystal phase, the PdTe NWs demonstrate a larger electrochemical surface area and higher poisoning tolerance, exhibiting enhanced EOR performances compared to the Pd–Te nanotubes. Electrochemical evaluations reveal that the PdTe NWs have excellent EOR activity of 4.4 A mg_{Pd}^{-1} in an alkaline medium. In addition, the method could be used to synthesize other hexagonal nanowires, *e.g.* $PtTe_2$.

Scheme 1 illustrates the template-directed synthesis of 1D PdTe NWs through a two-step hydrothermal process (see Experimental section for details). Initially, the Te NWs were synthesized *via* a typical hydrothermal method.[12] As shown in Fig. S1a–c of the ESI,† for the transmission electron microscopy (TEM) images with different magnifications, uniform Te NWs are obtained with an average diameter of *ca.* 15.6 nm, as seen in Fig. S2 (ESI†) for the histogram showing

---

[a] *State Key Laboratory of Mesoscience and Engineering, Institute of Process Engineering, Chinese Academy of Sciences, Beijing 100190, China. E-mail: sntian@ipe.ac.cn, jyang@ipe.ac.cn*
[b] *Center of Materials Science and Optoelectronics Engineering, University of Chinese Academy of Sciences, Beijing 100049, China*
[c] *School of Chemistry and Materials Science, Jiangsu Key Laboratory of New Power Batteries, Jiangsu Collaborative Innovation Centre of Biomedical Functional Materials, Nanjing Normal University, Nanjing 210023, China. E-mail: xulin001@njnu.edu.cn*

† Electronic supplementary information (ESI) available: Experimental details, tables, and additional figures associated with the evaluation and characterization of the samples prepared in this study. See DOI: https://doi.org/10.1039/d4cc04496g

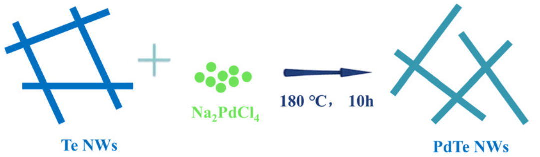

Scheme 1 Schematic illustration showing the template-directed synthesis of PdTe NWs through a two-step hydrothermal process.

the diameter statistics. The high-resolution TEM (HRTEM) image shown in Fig. S1d (ESI†) suggests a lattice fringe of 0.323 nm, corresponding to the (011) facet of hexagonal Te. The XRD pattern of the Te NWs also matches the hexagonal Te reference (JCPDS 86-2268) very well, as confirmed by Fig. S1e (ESI†). Fig. S3 (ESI†) shows the energy-dispersive X-ray (EDX) spectroscopy results, in which only the Te element presents besides carbon and copper signals from the sample holder, also supporting the successful synthesis of Te NWs.

Subsequently, the Te NWs were used as templates to prepare PdTe NWs. Fig. 1a–c displays the typical TEM images of the as-prepared PdTe NWs with different magnifications, which maintain the 1D morphology of the Te templates, with an average diameter of *ca.* 16.2 nm (see Fig. S4, ESI† for the particle size histogram of the PdTe NWs). In addition, an analysis of the HRTEM image (Fig. 1d) indicates a lattice fringe of 0.302 nm, corresponding to the (101) facet of the hexagonal PdTe phase. EDX spectroscopy (Fig. S5, ESI†) shows a Pd/Te atomic ratio of *ca.* 0.48/0.52, close to the stoichiometric ratio of the elements in the PdTe sample. The XRD pattern (Fig. 1e) verifies the hexagonal structure of the PdTe NWs (JCPDS 29-0971), with a discernible diffraction peak at 27.5° attributable to the residual Te from the templates. Furthermore, the EDX-based element maps (Fig. 1f–i) demonstrate that Pd and Te distribute evenly throughout the wire-like sample, definitely supporting the successful synthesis of PdTe NWs with the homogeneous hexagonal phase.

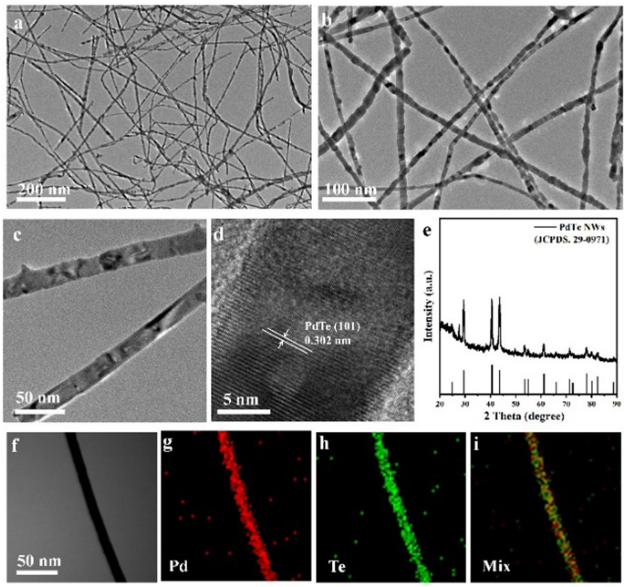

Fig. 1 (a)–(c) TEM images with different magnifications, (d) HRTEM image, (e) XRD pattern, and (f)–(i) STEM and corresponding EDX-based element maps of the PdTe NWs.

To elucidate the reaction mechanism for forming hexagonal PdTe nanowires in a high-temperature polyol system, a morphological-evolution study was conducted by quenching the reaction system at various time intervals. As shown in Fig. S6a–c (ESI†), some small Pd nanoparticles are initially observed on the surfaces of the Te NWs at early stages. Subsequently, the particles on the surface of the nanowires gradually disappear, accompanied by the homogenization of the nanowires, proving that Pd atoms and Te atoms interdiffuse to form PdTe nanowires (Fig. S6d–f, ESI†). As schematically shown in Fig. S7 (ESI†), we speculate that the reaction mechanism for forming hexagonal PdTe nanowires between the Pd precursor and Te nanowires involves: (i) the $PdCl_4^{2-}$ precursor is reduced to individual Pd nanoparticles in a high-temperature polyol system, which deposits on the surface of the Te NWs; (ii) subsequently, the interdiffusion (also called Kirkendall effect) of Pd and Te atoms occurs due to their close electronegativity (Pd: 2.2; Te: 2.1) and similar atomic radii (Pd: 1.37 Å; Te: 1.70 Å) to form alloy PdTe NWs.

X-ray photoelectron spectroscopy (XPS) was conducted to investigate the electronic interaction between Te and Pd. The XPS full spectrum and high-resolution Pd 3d and Te 3d spectra of the PdTe NWs are shown in Fig. S8 and S9 (ESI†). Compared to commercial Pd/C, the Pd 3d binding energies of the PdTe NWs are slightly lower, suggesting slight electron shift from Te to Pd in the PdTe NWs,[6d,7b] and this shift could be attributed to the electronegativity differences between Pd (2.20) and Te element (2.10).

The changes in electronic properties of Pd in the PdTe NWs would inevitably affect their electrocatalysis in typical electrochemical reactions by altering the adsorption and desorption of reaction intermediates. Before the electrochemical tests, the PdTe NWs were loaded on a commercial Vulcan XC-72R substrate by sonication. Fig. S10 (ESI†) shows the TEM image of the carbon-supported PdTe NWs (labeled as PdTe NWs/C). The cyclic voltammetry (CV) curves were recorded for both PdTe NWs/C and commercial Pd/C in 1 M KOH solution. As shown in Fig. S11 (ESI†), the peaks observed from 0.6 to 0.9 V are assigned to the reduction of the Pd oxide layer on the catalyst surface,[13] while the peak at 0.98 V for the PdTe NWs/C is attributed to the oxidation of Te.[7b] The PdO peak of the PdTe NWs/C shifts positively in comparison with that of commercial Pd/C, which implies that the active sites exposed on the PdTe NWs/C are easier to recover.[14] Considering that the Pd oxidation might reach the sublayer or even deeper into the crystals, the electrochemical active surface areas (ECSAs) of these catalysts were evaluated by stripping a Cu monolayer that was deposited on the electrode through the Cu underpotential deposition (Cuupd) method.[15] The CV curves for Cuupd experiments are shown in Fig. S12 (ESI†), and the ECSAs determined from the Cuupd method are 46.9 and 38.3 $m^2\ g^{-1}$, respectively, as listed in Table S1 and Fig. S13 (ESI†). The higher ECSA of the PdTe NWs/C than that of the Pd/C catalyst could be attributed

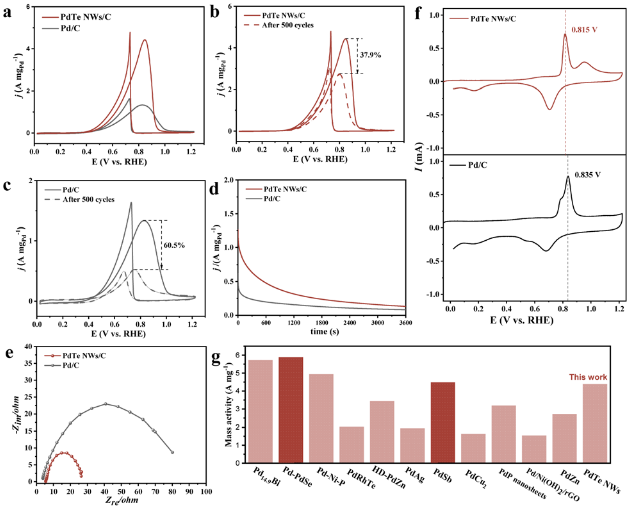

Fig. 2 (a) CVs of the PdTe NWs/C and Pd/C for the EOR in 1 M KOH + 1 M ethanol solution; CVs of (b) the PdTe NWs/C and (c) Pd/C before and after 500 cycles; (d) chronoamperometric tests showing the stability of the catalysts; (e) electrochemical impedance spectroscopy; (f) CV curves of CO stripping in 1 M KOH solution; (g) comparison between Pd Te NWs/C and other reported Pd-based EOR catalysts.

to the rough surfaces of the 1D nanowires, which could facilitate the electrocatalytic oxidation of ethanol molecules.

As expected, the PdTe NWs/C exhibit higher current density for the EOR in 1 M KOH + 1 M CH_3CH_2OH electrolyte. As displayed in Fig. 2a, two characteristic oxidation peaks are identified from the CV curves, in which the peak in the forward scan is associated with ethanol oxidation, while the peak in the reverse scan originates from further oxidation or removal of the poisoning carbonaceous intermediates.[16] Notably, the PdTe NWs/C show much higher mass activity (4.4 A mg_{Pd}^{-1}) than that of the commercial Pd/C catalyst (1.3 A mg_{Pd}^{-1}). We also normalized the activities by the ECSA to obtain the specific activity. Again, the PdTe NWs/C show better EOR performance (9.4 mA cm^{-2}) relative to the Pd/C catalyst (3.4 mA cm^{-2}), as observed in Fig. S14 (ESI†). To make it easier for comparison, the mass and specific activities of relevant catalysts are summarized in Fig. S15 and Table S1 (ESI†). The stability of the catalysts is also an essential factor to evaluate the electrocatalytic performance. The stability of the PdTe NWs/C and Pd/C was examined by continuous CV scans in ethanol-containing electrolyte. As depicted in Fig. 2b and c, the PdTe NWs/C show an activity decrease by 37.9% in the CV curves after 500 cycles. In contrast, the activity of the commercial Pd/C catalyst sharply decreases by 60.5% after 500 cycles, probably due to its easy CO contamination and particle aggregation.[17] In addition, chronoamperometry (CA) was employed as another method to estimate the stability of the PdTe NWs/C and Pd/C catalyst. As shown in Fig. 2d, the PdTe NWs/c demonstrate a higher current density compared with Pd/C, further verifying their better stability. Furthermore, ten consecutive cycles of PdTe NWs/C in a fresh 1 M KOH containing 1 M ethanol solution were conducted. As shown in Fig. S16 (ESI†), there is no significant decrease in the initial mass activity of the PdTe NWs/C.

The PdTe NWs/C after the stability test were characterized by TEM. As revealed by the TEM image (Fig. S17, ESI†), negligible change is observed in the morphology and sizes for the PdTe sample. The corresponding composition change was detected by EDX. As shown in Fig. S18 (ESI†), the Pd/Te atomic ratio is 0.57/0.43, with subtle change compared with the original one. Furthermore, EDX-based element maps of the PdTe NWs/C after the stability test prove that the Pd and Te elements retain a uniform distribution in the nanowires (Fig. S19, ESI†), also confirming higher catalytic stability of the PdTe NWs/C towards ethanol electrooxidation.

To further elucidate the reasons behind the enhanced EOR catalysis, electrochemical impedance spectroscopy (EIS) of the catalysts for the EOR was investigated. The PdTe NWs/C exhibit a smaller impedance arc radius in comparison with that of the Pd/C catalyst (Fig. 2e), indicating their lower charge-transfer resistance.[18] Additionally, electrochemical CO stripping curves (Fig. 2f) demonstrate that the peak potential of CO stripping on the PdTe NWs/C (0.815 V) is more negative than that on Pd/C (0.835 V), suggesting that the former possesses better CO_{ads} intermediate tolerance.[19] It has been well documented that ethanol oxidation includes C1 and C2 pathways. The EOR selectivity of Pd for the C1 pathway has been uncovered to be very low (<7.5%).[5] However, previous studies reveal that the introduction of Te into Pd significantly improves the C1 selectivity of the EOR process (56.6% or higher).[6d] The good CO tolerance on PdTe NWs is beneficial to eliminate the toxic intermediate species such as CO_{ad} and CH_x generated in the C1 process, thus promoting the C1 pathway. In addition, the 1D feature of the PdTe NWs provides a large surface area, delivering more active sites for electrochemical reactions, thus enhancing the EOR performance.[20] Also, as summarized in Fig. 2g and Table S2 (ESI†), the remarkable mass activity of the PdTe NWs/C also outperforms that of many reported Pd-based EOR electrocatalysts. Moreover, the PdTe NWs/C also exhibit relatively higher catalytic activity for the methanol oxidation reaction (MOR) and ethylene glycol oxidation reaction (EGOR) in an alkaline medium, as shown in Fig. S20 and S21 (ESI†).

Impressively, the template-directed synthesis can be extended to produce other metal–Te systems. With Te as the template, high-quality $PtTe_2$ nanowires (donated as $PtTe_2$ NWs) have been successfully fabricated. Fig. 3a–c presents the typical TEM images of the as-obtained $PtTe_2$ NWs with 1D morphology. The clear lattice fringe of 0.289 nm in the HRTEM image could be indexed to the (101) facet of the hexagonal $PtTe_2$ phase (Fig. 3d). The EDX analyses (Fig. S22, ESI†) testify an appropriate 1/2 ratio for Pt/Te in the as-prepared $PtTe_2$ NWs/C. The XRD pattern in Fig. 3e verifies the hexagonal phase of the synthesized $PtTe_2$ NWs. EDX-based element maps give rise to uniform distribution of Pt and Te in the nanowires (Fig. 3f–i), corroborating the successful synthesis of homogeneous $PtTe_2$ NWs using Te NWs as the template.

In summary, we have developed a template-directed synthesis of one-dimensional hexagonal PdTe nanowires. The hexagonal PdTe nanowires show excellent EOR electrocatalysis in an alkaline medium with a specific activity of 9.4 mA cm^{-2} and mass activity of 4.4 A mg_{Pd}^{-1}. Furthermore, this method could

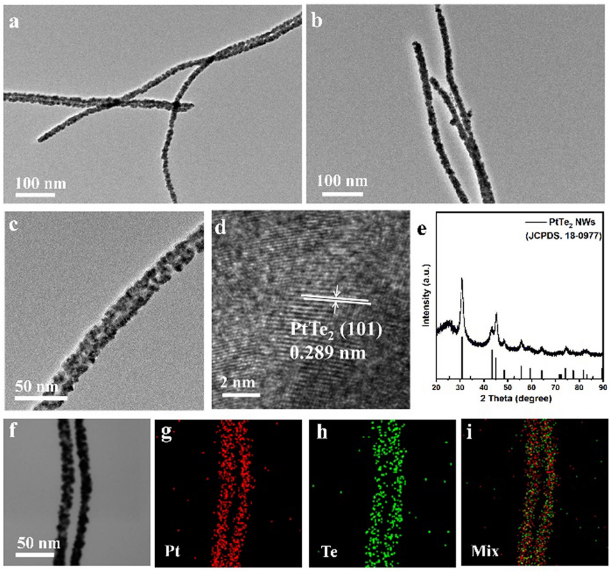

Fig. 3 (a)–(c) TEM images, (d) HRTEM image, (e) XRD pattern, and (f)–(i) STEM and corresponding EDX-based element maps of the $PtTe_2$ NWs.

be extended to synthesize hexagonal $PtTe_2$ nanowires. This work emphasizes composition and morphology tuning in designing efficient electrocatalysts for typical electrochemical reactions and gives rise to the construction of one-dimensional noble metal-based nanostructures.

We gratefully acknowledge the financial support from the National Natural Science Foundation of China (22272179, 22075290), CAS Project for Young Scientists in Basic Research (YSBR-044), and State Key Laboratory of Mesoscience and Engineering, Institute of Process Engineering, Chinese Academy of Sciences (MESO-23-A06, MESO-24-A01).

Data availability

The data supporting this article have been included as part of the ESI.†

Conflicts of interest

There are no conflicts to declare.

Notes and references

1 (*a*) W. Yan, G. Li, S. Cui, G.-S. Park, R. Oh, W. Chen, X. Cheng, J.-M. Zhang, W. Li, L.-F. Ji, O. Akdim, X. Huang, H. Lin, J. Yang, Y.-X. Jiang and S.-G. Sun, *J. Am. Chem. Soc.*, 2023, **145**, 17220; (*b*) J. Chang, G. Wang, X. Chang, Z. Yang, H. Wang, B. Li, W. Zhang, L. Kovarik, Y. Du, N. Orlovskaya, B. Xu, G. Wang and Y. Yang, *Nat. Commun.*, 2023, **14**, 1346.

2 (*a*) J. Chang, G. Wang, C. Li, Y. He, Y. Zhu, W. Zhang, M. Sajid, A. Kara, M. Gu and Y. Yang, *Joule*, 2023, **7**, 587; (*b*) X. Wang, H. Yang, M. Liu, Z. Liu, K. Liu, Z. Mu, Y. Zhang, T. Cheng and C. Gao, *ACS Nano*, 2024, **18**, 18701.

3 (*a*) D. Liu, Q. Zeng, C. Hu, H. Liu, D. Chen, Y. Han, L. Xu and J. Yang, *ACS Catal.*, 2022, **12**, 9092; (*b*) D. Liu, Y. Zhang, H. Liu, P. Rao, L. Xu, D. Chen, X. Tian and J. Yang, *Carbon Energy*, 2023, **5**, e324; (*c*) M. Zhang, X. Zhang, M. Lv, X. Yue, Z. Zheng and H. Xia, *Small*, 2023, **19**, 2205781.

4 (*a*) Y. Qiu, J. Zhang, J. Jin, J. Sun, H. Tang, Q. Chen, Z. Zhang, W. Sun, G. Meng, Q. Xu, Y. Zhu, A. Han, L. Gu, D. Wang and Y. Li, *Nat. Commun.*, 2021, **12**, 5273; (*b*) Y. Zhang, X. Liu, T. Liu, X. Ma, Y. Feng, B. Xu, W. Cai, Y. Li, D. Su, Q. Shao and X. Huang, *Adv. Mater.*, 2022, **34**, 2202333; (*c*) D. Liu, S. Tian, Y. Zhang, C. Hu, H. Liu, D. Chen, L. Xu and J. Yang, *ACS Appl. Energy Mater.*, 2023, **6**, 1459; (*d*) H. Wang, L. Jiao, L. Zheng, Q. Fang, Y. Qin, X. Luo, X. Wei, L. Hu, W. Gu, J. Wen and C. Zhu, *Adv. Funct. Mater.*, 2021, **31**, 2103465; (*e*) N. Ye, W. Sheng, R. Zhang, B. Yan, Z. Jiang and T. Fang, *Small*, 2024, **20**, 2304990.

5 F. Lv, W. Zhang, M. Sun, F. Lin, T. Wu, P. Zhou, W. Yang, P. Gao, B. Huang and S. Guo, *Adv. Energy Mater.*, 2021, **11**, 2100187.

6 (*a*) Y. Qin, W. Zhang, F. Wang, J. Li, J. Ye, X. Sheng, C. Li, X. Liang, P. Liu, X. Wang, X. Zheng, Y. Ren, C. Xu and Z. Zhang, *Angew. Chem., Int. Ed.*, 2022, **61**, e202200899; (*b*) H. Jia, N. Yao, J. Zhu, Y. Liu, Y. Lao, H. Cong and W. Luo, *Chin. J. Struct. Chem.*, 2022, **41**, 2208031; (*c*) J. Yu, B. Chang, W. Yu, X. Li, D. Wang, Z. Xu, X. Zhang, H. Liu and W. Zhou, *Carbon Energy*, 2022, **4**, 237; (*d*) L. Wang, Z. Yu, W. Yan, L. Liu, M. Wang, Q. Kong, Z. Hu, H. Geng, X. Huang and Y. Li, *Appl. Catal., B*, 2024, **343**, 123564.

7 (*a*) Y. Xu, D. Wu, P. Deng, J. Li, J. Luo, Q. Chen, W. Huang, C. M. Shim, C. Jia, Z. Liu, Y. Shen and X. Tian, *Appl. Catal., B*, 2022, **308**, 121223; (*b*) X. Huang, B. Xu, J. Feng, S. Hu, W. Dou, T. Yang, C. Zhan, S. Liu, Y. Ji, Y. Li, C.-W. Pao, Z. Hu, Q. Shao and X. Huang, *J. Am. Chem. Soc.*, 2023, **145**, 28010; (*c*) X. Tian, X. Zhao, Y.-Q. Su, L. Wang, H. Wang, D. Dang, B. Chi, H. Liu, E. J. M. Hensen, X. W. Lou and B. Y. Xia, *Science*, 2019, **366**, 850.

8 (*a*) X. Chu, J. Li, H. Xu and W. Qian, *Dalton Trans.*, 2023, **52**, 245; (*b*) G.-Q. Liu, Y. Yang, X.-L. Zhang, H.-H. Li, P.-C. Yu, M.-R. Gao and S.-H. Yu, *Small*, 2024, **20**, 2306914.

9 S.-Y. Ma, H.-H. Li, B.-C. Hu, X. Cheng, Q.-Q. Fu and S.-H. Yu, *J. Am. Chem. Soc.*, 2017, **139**, 5890.

10 L. Li, P. Wang, Z. Cheng, Q. Shao and X. Huang, *Nano Res.*, 2022, **15**, 1087.

11 L. Jin, H. Xu, C. Chen, H. Shang, Y. Wang and Y. Du, *Inorg. Chem.*, 2019, **58**, 12377.

12 H. W. Liang, S. Liu, J.-Y. Gong, S.-B. Wang, L. Wang and S.-H. Yu, *Adv. Mater.*, 2009, **21**, 1850.

13 W. Du, K. E. Mackenzie, D. F. Milano, N. A. Deskins, D. Su and X. Teng, *ACS Catal.*, 2012, **2**, 287.

14 (*a*) H. Liu, C. Koenigsmann, R. R. Adzic and S. S. Wong, *ACS Catal.*, 2014, **4**, 2544; (*b*) Q. Zeng, D. Liu, H. Liu, P. Cui, C. Hu, D. Chen, L. Xu, X. Wu and J. Yang, *iScience*, 2021, **24**, 103332.

15 (*a*) J. Okada, J. Inukai and K. Itaya, *Phys. Chem. Chem. Phys.*, 2001, **3**, 3297; (*b*) M. Luo, Z. Zhao, Y. Zhang, Y. Sun, Y. Xing, F. Lv, Y. Yang, X. Zhang, S. Hwang, Y. Qin, J.-Y. Ma, F. Lin, D. Su, G. Lu and S. Guo, *Nature*, 2019, **574**, 81.

16 X. Li, H. You, C. Wang, D. Liu, R. Yu, S. Guo, Y. Wang and Y. Du, *J. Colloid Interface Sci.*, 2021, **591**, 203.

17 S. Huang, S. Lu, H. Hu, F. Xu, H. Li, F. Duan, H. Zhu, H. Gu and M. Du, *Chem. Eng. J.*, 2021, **420**, 130503.

18 (*a*) Z. Hu, Y. Zhang, L. Xu, J. Zhong, H. Liu, S. Tian and J. Yang, *Inorg. Chem.*, 2023, **62**, 5707; (*b*) W. Qiao, M. Zha, Y. Yang, G. Hu and L. Feng, *Chem. Commun.*, 2022, **58**, 10651.

19 (*a*) Z. Qin, A. Fan, Q. Zeng, D. Chen, Z. Hu, H. Liu, P. Cui and J. Yang, *ACS Appl. Energy Mater.*, 2023, **6**, 5607; (*b*) Y. Wang, M. Zheng, Y. Li, C. Ye, J. Chen, J. Ye, Q. Zhang, J. Li, Z. Zhou, X.-Z. Fu, J. Wang and S.-G. Sun, *Angew. Chem., Int. Ed.*, 2022, **61**, e202115735.

20 K. Yin, Y. Chao, F. Lv, L. Tao, W. Zhang, S. Lu, M. Li, Q. Zhang, L. Gu, H. Li and S. Guo, *J. Am. Chem. Soc.*, 2021, **143**, 10822.